Computers and Electrical Engineering 119 (2024) 109511

Contents lists available at ScienceDirect

Computers and Electrical Engineering

journal homepage: www.elsevier.com/locate/compeleceng

Design procedures for series–series wpt systems: A comparative analysis

Fabio Corti [a,*], Vittorio Bertolini [b], Antonio Faba [b], Ermanno Cardelli [b], Alberto Reatti [a]

[a] University of Florence, Italy
[b] University of Perugia, Italy

ARTICLE INFO

Keywords:
Inductive wireless power transfer
Design procedure
Misalignment
Extended describing function

ABSTRACT

The Series–Series (SS) compensation is one of the most commonly employed topologies for enhancing the efficiency of Wireless Power Transfer (WPT) systems. In this topology, two capacitors are connected in series with the transmitter and receiver coils.

Currently, in the literature, these capacitors are tuned to resonate with the self-inductance of the coils at the nominal frequency. Anyway, analyzing the circuit, another interesting possibility emerges: the calibration of the capacitors to resonate with the leakage inductances of the coupled coils. This approach, currently not investigated in the literature, leads to a system with significantly different characteristics.

A comparative analysis between these two methods is lacking in the literature. Therefore, this paper aims to fill this gap by proposing an in-depth comparison between the two design procedures, with the aim of providing useful insights to designers in selecting the most appropriate design technique for their application. The analysis includes both steady-state and transient conditions. In particular, the input impedance, voltage transfer function and the transmission efficiency at different frequencies and coupling coefficients are compared.

The theoretical results are validated experimentally. The results obtained are extremely interesting and are particularly useful for selecting the most appropriate sizing technique for a given application during the design phase.

1. Introduction

Inductive Wireless power transfer (IWPT) systems are widely used as a suitable solution for charging devices without direct connections. Since the power is transferred across a large air gap, the coupling coefficient between the magnetically coupled coils is typically low. To increase the transmission efficiency, resonance compensation is required to operate in resonance and minimize the reactive power [1]. These compensations consist of additional reactive components, such as capacitors and inductors, connected to the primary and secondary coils. Several resonant topologies have been proposed over the years. Detailed overviews are given in [2,3].

The SS compensation allows high efficiency even at low coupling coefficients, making it well suited for applications such as electric vehicle charging [4]. In addition, the secondary current remains largely unaffected by load variations, making it easier to control the charging process [5]. This compensation consists of connecting two capacitors, called C_p and C_s, in series with the primary and secondary windings, as shown in Fig. 1. The capacitors are then calibrated to resonate at a specific nominal frequency f_n. This condition allows to minimize the reactive power absorbed by the circuit and therefore to maximize the efficiency [6].

* Corresponding author.
E-mail address: fabio.corti@unifi.it (F. Corti).

https://doi.org/10.1016/j.compeleceng.2024.109511
Received 2 January 2024; Received in revised form 19 July 2024; Accepted 22 July 2024
Available online 5 August 2024

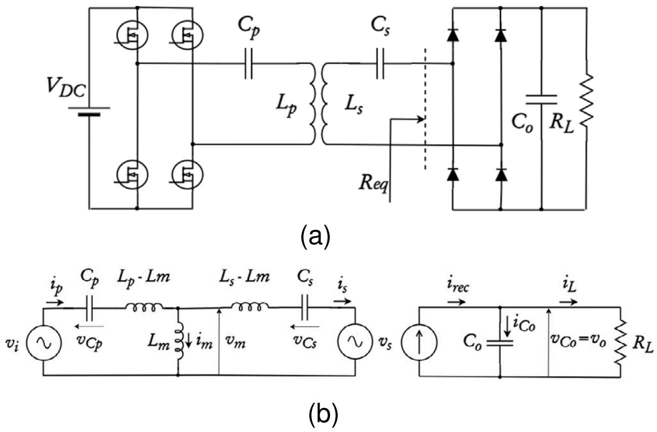

Fig. 1. WPT circuit topology. (a) DC–DC electric circuit. (b) Equivalent model..

Currently, in the literature, the resonance condition is achieved by calibrating the two capacitances C_p^{P1} and C_s^{P1} in order to resonate with the self-inductances of the primary and secondary coils L_p and L_s at the nominal operating angular frequency $\omega_n = 2\pi f_n$. Thus, capacitances and inductances are related by [7–13]

$$C_p^{P1} = \frac{1}{\omega_n^2 L_p}, \quad C_s^{P1} = \frac{1}{\omega_n^2 L_s} \tag{1}$$

This design approach, which represents the actual state of the art, is referred to as $P1$ in this paper.

Analyzing the circuit shown in Fig. 1, another interesting design possibility emerges: the calibration of the two capacitances C_p^{P2} and C_s^{P2} to resonate with the primary and secondary leakage inductances L_{kp} and L_{ks}. In this case, the capacitances and the inductances are related by

$$C_p^{P2} = \frac{1}{\omega_n^2 L_{kp}} = \frac{1}{\omega_n^2 (1-k) L_p}, \quad C_s^{P2} = \frac{1}{\omega_n^2 L_{ks}} = \frac{1}{\omega_n^2 (1-k) L_s} \tag{2}$$

This second design method, called $P2$, is almost completely unexplored in the literature. After an extensive search of the literature, only [14,15] have used $P2$ to achieve a constant voltage gain independent of the load at a constant frequency. However, there is no comparison with $P1$ and the analysis is limited to steady-state conditions. In addition, the effects of coupling coefficient variation are not analyzed.

From (1) and (2) it is clear that these two approaches lead to similar results when the system operates with a low coupling coefficient ($k < 0.2$), for example for electric vehicle wireless charging [16,17]. However, for higher coupling coefficients, such as for consumer electronics applications [18,19], the behavior of these two procedures can significantly diverge and this difference is currently unexplored in the literature.

For this reason, this paper aims to clarify the consequences of using two different design techniques. The goal is to highlight the characteristics of each technique both under steady-state and transient conditions.

To this end, the model of the entire converter will be initially derived using the Extended Describing Function (EDF), which represents one of the most commonly used techniques for extrapolating steady-state and small-signal models for resonant converters.

Once the model is developed, the characteristics of the system designed using $P1$ and $P2$ will be compared. As will be shown in detail in the following Sections, the main interesting and non-trivial results emerging from this study can be summarized as follows:

(1) Procedure $P1$ ensures operating at maximum transmission efficiency at the nominal operating frequency f_n. This is because the phase of the input impedance of the compensating network is always zero at the nominal operating frequency f_n.
(2) Procedure $P2$ allows the output voltage to be strongly independent of the coupling coefficient at the nominal frequency f_n while using procedure $P1$, the output voltage is highly sensitive to changes in the coupling coefficient k.
(3) Procedure $P2$ leads to a lower harmonic content of voltage and current independently of the coupling coefficients. This allows the use of the First Harmonic Approximation (FHA) hypothesis without significant errors, making the EDF model particularly accurate. On the other hand, procedure $P1$ is characterized by significant harmonic contents, compromising the accuracy of the EDF model and, therefore, reducing the performance of the closed-loop system.

These three main results are particularly important and can assist the designer in selecting the most suitable sizing technique for their application.

For example, for those applications where efficiency is the most important aspect, such as biomedical implants where the leakage magnetic field must be minimized for safety reasons and therefore the efficiency must be maximized, the choice of the $P1$ procedure is recommended.

On the other hand, if the application is characterized by a large possibility of misalignments, the $P2$ procedure is preferable to allow greater stability of the output voltage. In addition, for those applications where electromagnetic interferences and noise-immunity is a key aspect, the procedure $P2$ is recommended due to its low harmonic contents.

Finally, for applications in which dynamic control is a key aspect, such as for the dynamic charging of electric vehicles in which the coupling coefficient varies quickly and rapid control is fundamental, the choice of the $P2$ procedure is preferable as it allows obtain more accurate dynamic models and therefore better-performing controls.

The paper is organized as follows. In Section 2, the large-signal model based on EDF is presented. This model, based on FHA, is the starting point for the derivation of the small-signal model required to design the controller. In Section 3, an extensive steady-state analysis of the voltage transfer function using the two procedures is presented. The aim of this section is to analytically derive the characteristics of the two procedures and compare their behavior. In Section 4, the experimental validation is carried out. Finally, in Section 5, the results are discussed in the conclusions.

2. Large signal model based on extended describing functions

2.1. Circuit topology

The electric circuit of the SS compensated WPT system is shown in Fig. 1(a). Modeling the coupled coils by the leakage inductances L_{kp} and L_{ks} and the magnetizing inductance L_m, and using the equivalent circuit of the rectifier presented in [20], the equivalent circuit shown in Fig. 1(b) can be obtained.

To derive the model based on the EDF the following steps have been observed :

(1) The Kirchhoff's voltage and current laws have been applied to the circuit of Fig. 1(a), deriving a general non-linear model [20].
(2) Assuming that the system operates close to the resonance, the First Harmonic Approximation (FHA) is used and all the currents and voltages in the circuits are assumed to be sinusoidal.
(3) All the variables involved in the model are expressed as a combination of sine and cosine terms. As a consequence, a new set of equations can be derived isolating among them the sine and cosine terms. The obtained set represents the Large Signal Model [20].
(4) From the Large Signal model, the Steady State and the Small Signal models are derived.

In the next subsections, these four steps are briefly summarized.

2.2. Kirchhoff's voltage and currents laws

The circuit shown in Fig. 1(a) can be described by the equations:

$$v_i = v_{cp} + L_{kp}\frac{di_p}{dt} + v_m = v_{cp} + L_{kp}\frac{di_p}{dt} + L_m\frac{di_m}{dt}, \tag{3}$$

$$v_m = L_m\frac{di_m}{dt} = L_{ks}\frac{di_s}{dt} + v_{cs} + v_s, \tag{4}$$

$$i_p = C_p\frac{d}{dt}v_{cp}, \tag{5}$$

$$i_s = C_s\frac{d}{dt}v_{cs}, \tag{6}$$

$$i_m = i_p - i_s, \tag{7}$$

$$i_{rec} = i_{Co} + i_L = C_o\frac{dv_{Co}}{dt} + \frac{v_o}{R_L}. \tag{8}$$

where v_{cp} and v_{cs} are the voltages across the capacitors C_p and C_s. Since the output voltage v_o is equal to the voltage across the output capacitor C_o, the expression of v_o can be derived from (8):

$$v_o = v_{Co} = R_L\left(i_{rec} - C_o\frac{dv_o}{dt}\right) \tag{9}$$

2.3. FHA and extended describing function model

The first step of the EDF approach consists of writing a generic current or voltage signal x in the form:

$$x = x_s(c_v)\sin(\omega_s t) + x_c(c_v)\cos(\omega_s t) \tag{10}$$

where c_v is a generic control variable such as the switching frequency or the duty cycle. It is interesting to note that the derivate of a signal written in this form can be calculated as

$$\begin{aligned}\frac{dx}{dt} &= \left[\frac{dx_s(c_v)}{dt} - \omega_s x_c\right]\sin(\omega_s t)\\ &+ \left[\frac{dx_c(c_v)}{dt} + \omega_s x_s\right]\cos(\omega_s t).\end{aligned} \tag{11}$$

Since in the circuit shown in Fig. 1 there are non-sinusoidal currents/voltages, the next step is to approximate them with their first harmonic. In particular, the voltages v_i and v_s are square waveforms, while the current i_{rect} is the absolute value of the sinusoidal current i_s.

Regarding the square voltage with a generic duty cycle D impressed by the inverter, it can be approximated by its first harmonic v_i using the Fourier series expansion as follows:

$$\begin{aligned}v_i(t) =& \Big[\frac{2}{\pi} m \sin(2\pi D)\cos\left(\omega_s t\right)\\ &+\frac{2}{\pi} m[1-\cos(2\pi D)]\sin\left(\omega_s t\right)\Big] V_{DC}\\ &= v_{is} sin(\omega_s t) + v_{ic} cos(\omega_s t)\end{aligned} \tag{12}$$

where and $v_{is} = \frac{2}{\pi} m[1 - cos(2\pi D)]V_{DC}$ and $v_{ic} = \frac{2}{\pi} m[sin(2\pi D)]V_{DC}$. The coefficient m is 1 if a full bridge is used while it is 0.5 if a half bridge is used.

Regarding v_s, neglecting the forward voltage of the diodes, it is a square wave with an amplitude equal to V_o. The first harmonic of v_s and the secondary current i_s are in-phase since the rectifier can be approximated by an equivalent load resistance $R_{eq} = \frac{8}{\pi^2} n^2 R_L$, as shown in Fig. 1(a). With this assumption, v_s can be written as:

$$v_s(t) = V_o sign(i_s(t)) = V_o \frac{i_s(t)}{|i_s(t)|}. \tag{13}$$

Applying the Fourier Series Expansion to (13), the first harmonic of v_s can be obtained:

$$v_s(t) = \frac{4}{\pi}\frac{i_{ss}}{i_k} v_o \sin\left(\omega_s t\right) + \frac{4}{\pi}\frac{i_{sc}}{i_k} v_o \cos\left(\omega_s t\right) \tag{14}$$

where i_k is the peak value of the secondary current and it is defined in (15).

The last signal which must be approximated as sinusoidal is the rectified current i_{rec}. This current is the absolute value of the secondary current, that is:

$$i_{rec} = |i_2| = \frac{2}{\pi} i_k = \frac{2}{\pi}\sqrt{i_{ss}^2 + i_{sc}^2}. \tag{15}$$

The factor $2/\pi$ is used to extract the mean value from a sinusoidal function.

2.4. Large signal, steady-state and small signal model

Substituting (10)–(15) to (3)–(6), four equations containing terms expressed with $sin(\omega_s t)$ and $cos(\omega_s t)$ can be obtained. Then, the sine and cosine terms can be divided, obtaining the following equations, which represent the large signal model:

$$\frac{di_{ps}}{dt} = \frac{1}{L_{eq2}} v_{es} - \frac{1}{L_{eq2}} v_{cps} - \frac{1}{L_{eqm}} v_{css} - \frac{1}{L_{eqm}}\frac{4}{\pi}\frac{i_{ss} v_o}{i_k} + \omega_s i_{pc}, \tag{16}$$

$$\frac{di_{ss}}{dt} = \frac{1}{L_{eqm}} v_{es} - \frac{1}{L_{eqm}} v_{ps} - \frac{1}{L_{e1}} v_{ss} - \frac{1}{L_{eq1}}\frac{4}{\pi}\frac{i_{ss} v_o}{i_k} + \omega_s i_{sc}, \tag{17}$$

$$\frac{dv_{ps}}{dt} = \frac{i_{ps}}{C_p} + \omega_s v_{pc}, \tag{18}$$

$$\frac{dv_{ss}}{dt} = \frac{i_{ss}}{C_s} + \omega_s v_{sc}, \tag{19}$$

$$\frac{di_{pc}}{dt} = \frac{v_{ec}}{L_{eq2}} - \frac{1}{L_{eq2}} v_{pc} - \frac{1}{L_{eqm}} v_{sc} - \frac{1}{L_{eqm}}\frac{4}{\pi}\frac{i_{ss} v_o}{i_k} - \omega_s i_{ps}, \tag{20}$$

$$\frac{di_{sc}}{dt} = \frac{v_{ec}}{L_{eqm}} - \frac{1}{L_{eqm}} v_{pc} - \frac{1}{L_{eq1}} v_{sc} - \frac{1}{L_{eq1}}\frac{4}{\pi}\frac{i_{ss} v_o}{i_k} - \omega_s i_{ss}, \tag{21}$$

$$\frac{dv_{pc}}{dt} = \frac{i_{pc}}{C_p} - \omega_s v_{ps}, \tag{22}$$

$$\frac{dv_{sc}}{dt} = \frac{i_{sc}}{C_s} - \omega_s v_{ss}, \tag{23}$$

Table 1
Wireless power transfer system characteristics.

Parametro	Valore
Operating frequency f_s	85 kHz
Duty cycle D	0.5
Input voltage V_{DC}	12 V
Primary side inductance L_p	95.65 μH
Secondary side inductance L_s	86.28 μH
Primary parasitic resistance r_p	0.73 Ω
Secondary parasitic resistance r_s	0.70 Ω
Nominal load resistance R_L	6.1 Ω
Output capacitor C_o	47 μF

where L_{eq1}, L_{eq2} and L_{eqm} are equivalent inductances defined as combination of the self inductances L_p, L_s and L_m, as shown in [20]. Finally, the last equation can be derived from (9):

$$\frac{dv_o}{dt} = \frac{1}{C_o R_L} v_o - \frac{2}{\pi C_o} i_k. \tag{24}$$

The generic large signal model variable x can be split into the steady-state X and small-signal $\hat{x}$:

$$x = X + \hat{x}. \tag{25}$$

The steady-state model can be obtained by setting the derivative (16)–(23) to zero. On the other hand, as shown in [20], the Small-Signal Model (SSM) can be obtained by rearranging the previous equations in the form:

$$\begin{cases} \frac{d}{dt}\hat{x} = A_{ss}\hat{x} + B_{ss}\hat{u} \\ \hat{y} = \hat{v}_o = C_{ss}\hat{x} \end{cases} \tag{26}$$

where $\hat{u}$ is the input of the small-signal model while $\hat{y}$ is the output. In this paper, the angular switching frequency is chosen as a control variable, thus $\hat{u} = \omega_s$ while, since the output voltage regulation is performed, the output is $\hat{y} = v_o$. The expression of the matrix A_{ss}, B_{ss} and C_{ss} are shown in [20]. As shown in [21], the input-to-output transfer function can be calculated as:

$$T_p(s) = \frac{y(s)}{\hat{u}(s)} = \frac{\hat{v}_o(s)}{\hat{\omega}_s(s)} = -C_{ss}\left[A_{ss} - sI\right]^{-1} B_{ss}. \tag{27}$$

Finally, using (27), a controller to reach a design phase margin can be easily designed.

3. Resonant compensation design procedures: a comparison

In this section, using the EDFs model previously presented, the steady-state behaviors of the system at different coupling coefficients using the two procedures $P1$ and $P2$ are evaluated. In particular, the comparison is carried out by evaluating the voltage transfer function $M_v = V_o/V_i$, the input impedance Z_{in} and the transmission efficiency η.

The characteristics of the SS WPT systems used in this paper are shown in Table 1.

As previously mentioned, the first design procedure $P1$ consists of designing the capacitors to resonate with the self-inductances at the nominal operating frequency f_n. Thus, the capacitors can be calculated by the equations:

$$C_p^{P1} = \frac{1}{\omega_n^2 L_p}, \quad C_s^{P1} = \frac{1}{\omega_n^2 L_s}. \tag{28}$$

On the other hand, the second procedure $P2$ consists of designing the capacitors to resonate with the leakage inductance. Thus, the capacitors can be calculated by the equations:

$$C_p^{P2} = \frac{1}{\omega_n^2 (1-k) L_p}, \quad C_s^{P2} = \frac{1}{\omega_n^2 (1-k) L_s}. \tag{29}$$

In order to compare the performance of an SS WPT system designed with $P1$ or $P2$, multiple designs at different operating conditions have been investigated.

In particular, the systems have been designed using (28) or (29) for three different coupling coefficients: $k = 0.1$, $k = 0.3$ and $k = 0.5$. These coupling coefficients have been obtained using two circular spiral coils with a diameter $D_o = 25$ cm and placing them at a distance of $d = 8$ cm, $d = 5$ cm and $d = 2$ cm respectively. The resonant capacitances calculated using $P1$ and $P2$ for different coupling coefficients are shown in Fig. 2. The difference between values calculated using the $P1$ and $P2$ procedures increases as the coupling increases. Since procedure $P1$ does not involve the coupling coefficients, the value of capacitances C_p^{P1} and C_s^{P1} are the same independently from the coupling.

Case	k	C_p^{P1}	C_p^{P2}
A	0.1	36.6 nF	40.7 nF
B	0.3	36.6 nF	52.4 nF
C	0.5	36.6 nF	73.3 nF

Case	k	C_s^{P1}	C_s^{P2}
A	0.1	40.6 nF	45.1 nF
B	0.3	40.6 nF	58.4 nF
C	0.5	40.6 nF	81.3 nF

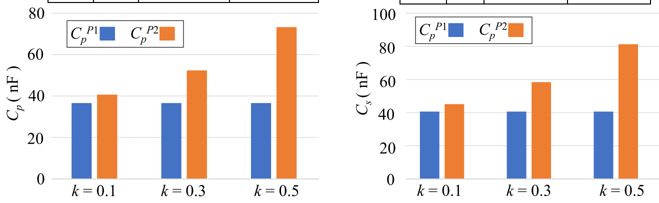

Fig. 2. Primary and secondary capacitances values using $P1$ and $P2$ for different coupling coefficients.

3.1. System analysis using the design procedure P1

Using the EDFs model introduced in Section 2, the steady-state voltage transfer function $M_v = V_o/V_i$ can be derived at different switching frequency f_s. In Fig. 3(a), the M_v is shown when the system is designed using $P1$ for the case A, B, C shown in Fig. 2 considering a nominal load resistance. From the phase plot of the input impedance Z_{in} shown in Fig. 3(c), it is clear that the resonant frequency f_0 occurs at the nominal frequency $f_n = 85$ kHz independently from the coupling coefficients k.

The procedure $P1$ becomes inconvenient for high coupling coefficients. In fact, as shown in Fig. 3(a), at the nominal frequency $f_n = 85$ kHz, the output voltage changes significantly as the coupling coefficient increases; increasing the coupling coefficient, the output voltage is drastically reduced. For this reason, for those applications where a stable output voltage is required in the presence of large variations in coupling coefficient, such as dynamic EV charging, the P1 procedure may be less suitable. Another drawback of the procedure $P1$ is the significative movement of the maxima of the voltage transfer function M_v away from the working frequency as the coupling coefficient increases, as shown in Fig. 3(a). In these conditions, the higher-order harmonics introduced by the inverter's square wave are not strongly filtered, producing distortion in the primary and secondary currents. This condition no longer validates the FHA assumption on which the EDF-based model is based.

As a consequence, the model presented in Section 2 based on the First Harmonic Approximation is no longer accurate, leading to a less robust small signal model and therefore complicating the design of the closed loop.

In Fig. 3(b)–(d) the same functions considered in Fig. 3(a)–(c) are evaluated when $R_L = 50\ \Omega$ (to make the results more generic). As can be seen, the trends are the same. The only important difference is that the absolute values for the V_o/V_i transfer function when k increases are quite high if compared with the corresponding ones when the nominal load resistance is considered (even if the evolution of the V_o/V_i function increasing k remain more or less the same). As consequence, it is expected that the higher harmonics had a smaller impact on the electric signals waveforms. The results of the efficiency trends (Fig. 3(e)–(f) will be discussed in the next paragraph, to make a direct comparison with the $P2$ strategy).

3.2. System analysis using the design procedure P2

First of all, a converter which works in with a nominal load resistance is considered. The voltage transfer function M_v using the design procedure $P2$ is shown in Fig. 4(a). Differently from the previous case, the resonant frequency f_0 does not correspond with the operating frequency $f_n = 85$ kHz. In fact, the Zero Phase Angle (ZPA) condition of the input impedance angle ϕ_{Zin} at $f_n = 85$ kHz (Fig. 4(c)) is almost reached for high coupling coefficients, while the impedance starts to be characterized by a significant angle for low coupling coefficients. A higher angle of the input impedance leads to a higher reactive power circulating in the compensation, reducing the transmission efficiency. In fact, the transmission efficiency η is reduced when operating with low coupling coefficients: since the input impedance has a significant phase, e.g. $\phi_{Zin} = -47°$, the circuit will absorb reactive power, increasing losses.

The $P2$ design procedure is particularly useful when operating with high coupling coefficients. As shown in Fig. 4(a), the voltage transfer function is particularly independent of the coupling coefficient at the operating frequency, i.e. $|M_v| = 1$, $\phi_v = 0$. This condition is suitable for those applications where the coupling coefficients can vary significantly during operation. For example, for charging mobile phones, where depending on the precision with which it is positioned there can be large variations in the coupling coefficient.

Concerning the efficiency, to better highlight the difference between $P1$ and $P2$ strategies, the efficiency at $f_1 = 75$ kHz, $f_2 = 85$ kHz and $f_3 = 95$ kHz (relatively to Figs. 3(e) and 4(e)) are reported in Table 2.

The main relevant aspect to underline is that the P2 strategy, especially working in resonant conditions (85 kHz), is able to grant the best stability in terms of output power and efficiency and also the higher output power as an absolute value. The highest efficiency occurs for the frequencies where the input impedance reaches its maximum, as visible in Figs. 3(c)–(d) and 4(c)–(d) since there is a limitation in the current (with a consequent limitation also in the power dissipation in the parasitic resistances). However, in this way, also the output power is limited (as shown also in Table 2).

Also in this case, Fig. 4(b),(d) and (f) show what happens using a load resistance $R_L = 50\ \Omega$: despite the obvious differences in terms of the specific values, the generic considerations made with the nominal load resistance are still valid.

The steady-state characteristics of the systems designed using $P1$ and $P2$ are compared and summarized in Table 3.

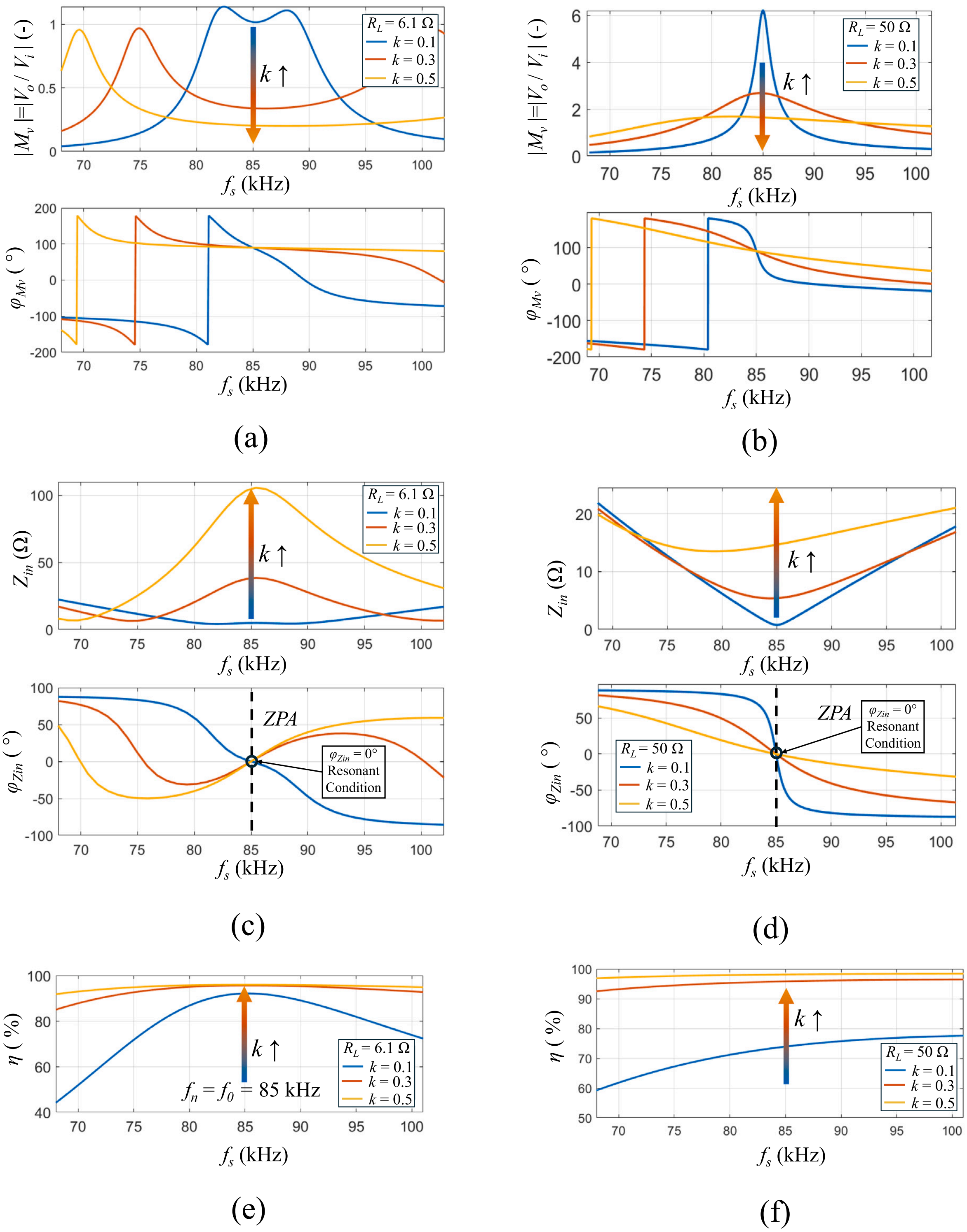

Fig. 3. Steady-state characteristics using $P1$ at different coupling coefficients. (a) Gain and phase of voltage transfer function M_v (nominal load resistance). (a) Gain and phase of voltage transfer functions M_v (R_L = 50 Ω) (c) Input impedance Z_{in} (nominal load resistance). (d) Input impedance Z_{in} (R_L = 50 Ω). (e) Transmission efficiency η (nominal load resistance). (f) Transmission efficiency η (R_L = 50 Ω).

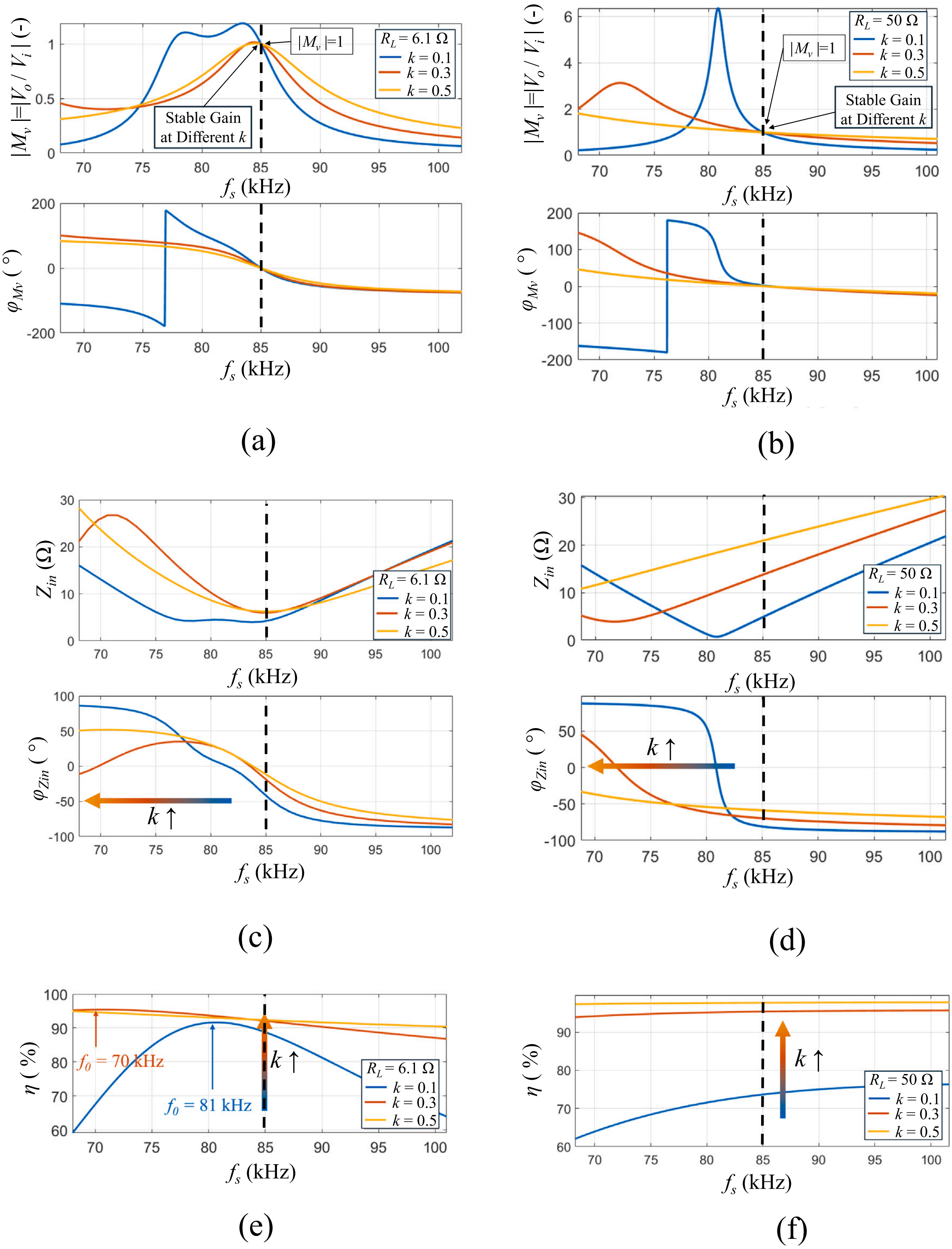

Fig. 4. Steady-state characteristics using $P2$ at different coupling coefficients. (a) Gain and phase of voltage transfer function M_v (nominal load resistance). (a) Gain and phase of voltage transfer functions M_v (R_L = 50 Ω) (c) Input impedance Z_{in} (nominal load resistance). (d) Input impedance Z_{in} (R_L = 50 Ω). (e) Transmission efficiency η (nominal load resistance). (f) Transmission efficiency η (R_L = 50 Ω).

Table 2
Efficiency of $P1$ and $P2$ strategies for different working frequencies.

k	f_1 = 75 kHz				f_2 = 85 kHz				f_3 = 95 kHz			
	P_1 (W)	η_1	P_2 (W)	η_2	P_1 (W)	η_1	P_2 (W)	η_2	P_1 (W)	η_1	P_2 (W)	η_2
0.1	0.25	0.72	2.48	0.85	11.25	0.92	10.05	0.89	0.76	0.82	0.18	0.73
0.3	9.57	0.93	2.14	0.95	1.35	0.96	10.09	0.92	2.97	0.94	0.7	0.89
0.5	1.30	0.95	2.32	0.94	0.49	0.96	10.10	0.92	0.55	0.95	1.57	0.91

Table 3
Characteristics of $P1$ and $P2$ systems.

Property	$P1$	$P2$
ZPA at the nominal frequency f_n (Maximum efficiency at $f_s = f_n$)	YES	NO
Voltage gain independent by coupling coefficient variation at f_n	NO	YES
Low current/voltage harmonic distortion and high accuracy of small-signal EDF model based on FH A	NO	YES

Table 4
Measured capacitances for $P1$ and $P2$ systems.

Capacitor	(A) k = 0.1	(B) k = 0.3	(A) k = 0.5
C_p^{P1}	36.2 nF	36.2 nF	36.2 nF
$ESR_{C_p^{P1}}$	29 mΩ	29 mΩ	29 mΩ
C_s^{P1}	41 nF	41 nF	41 nF
$ESR_{C_s^{P1}}$	38 mΩ	38 mΩ	38 mΩ
C_p^{P2}	40.3 nF	51 nF	69.5 nF
$ESR_{C_p^{P2}}$	28 mΩ	58 mΩ	48 mΩ
C_s^{P2}	46.5 nF	59.3 nF	80.7 nF
$ESR_{C_s^{P2}}$	32 mΩ	64 mΩ	78 mΩ

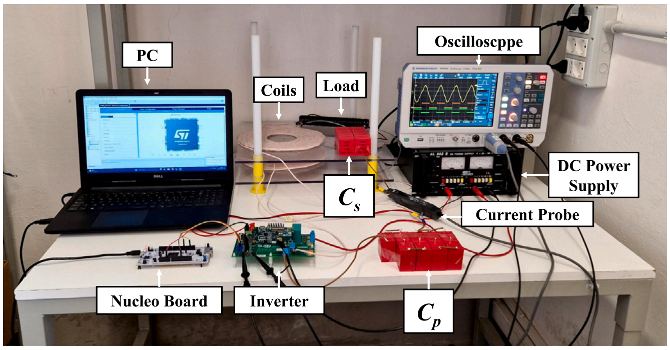

Fig. 5. Experimental setup.

4. Experimental validation

In order to experimentally validate the characteristics outlined in the previous Section, a laboratory setup capable of reproducing all the scenarios presented in Fig. 2 was implemented. In this way, thanks to this system, it is possible to assess and experimentally compare the characteristics of the two sizing techniques. The experimental setup is shown in Fig. 5.

The system constraints are shown in Table 1. Three different capacitors by WIMA have been used to create the capacitances calculated in (28) and (29): the FKP1U033307K00MSC9 (C = 33 nF), the FKP1O121005B00KSSD (C = 10 nF) and FKP1O114704C00JSSD (C = 4.7 nF).

All of these capacitors have a maximum AC voltage of 600 V, which is cautionary enough for this application.

A TTi LCR400 has been used to measure the capacitance value and the external series resistance (ESR) at the operating frequency. The results are shown in Table 4.

A GS665EVBMB evaluation board, that includes two GaN Systems GS66508T 650 V GaN Enhancement-mode HEMTs (E-HEMTs), has been used as half-bridge inverter. Once the setup has been realized, multiple steady-state and transient analyses have been performed as shown in the following sub-sections.

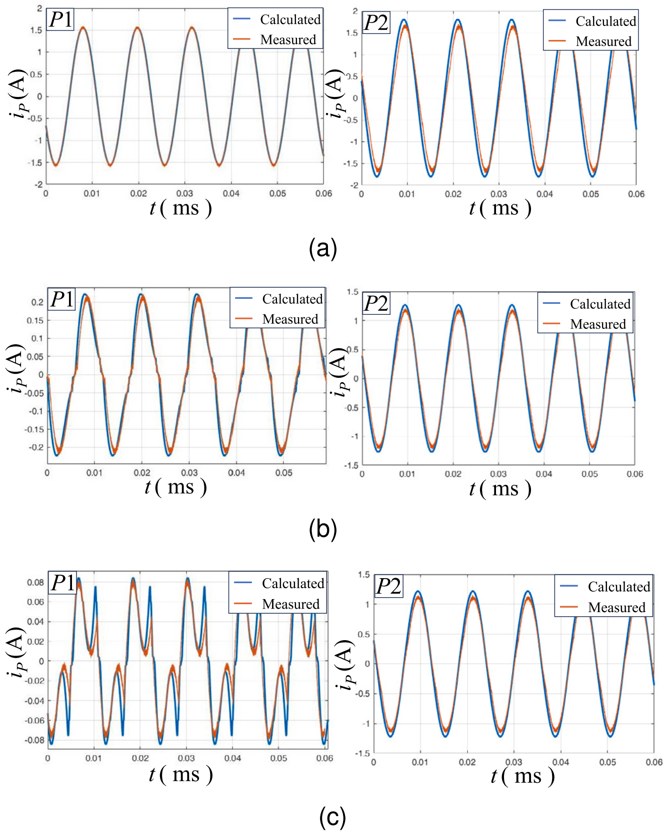

Fig. 6. Comparison between measured and predicted primary current using $P1$ and $P2$ design procedures. (a) $k = 0.1$; (b) $k = 0.3$; (c) $k = 0.5$.

4.1. Steady-state validation

This first analysis aims to understand how the choice of procedures $P1$ and $P2$ affect the validity of the first harmonic approximation (FHA).

The results are shown in Figs. 6 and 7, where the distortion of the primary current is evaluated for different coupling coefficients and load resistance.

For low coupling coefficients, e.g. $k = 0.1$ in Fig. 6(a), the current is approximately sinusoidal both for $P1$ and $P2$. As expected, according to Figs. 3(a) and 4(a), the two design procedures provide similar results for low coupling coefficients. Indeed, the quite high value of M_v, allows to completely filter higher harmonics.

Increasing the coupling coefficients, e.g. $k = 0.5$ in Fig. 6(c), the $P1$ system is affected by higher harmonic distortion. This is in line with theory; indeed, as shown in Fig. 3(a), the maximum of the transfer function M_v shifts away from the nominal frequency $f_n = 85$ kHz, reducing the filtering effect and increasing the presence of harmonics. On the other hand, using $P2$, the maximum is always close to the operating frequency $f_n = 85$ kHz, as shown in Fig. 4(a). As a consequence, the current shows a sinusoidal waveform for every value of the coupling coefficient, as shown in Fig. 6. A parallel analysis has been performed considering as load resistance $R_L = 50\ \Omega$. Results are shown in Fig. 7. The $P2$ strategy provides results which are quite similar to those ones found using a nominal load resistance. Indeed, also in this case, as shown in Fig. 4(b), $M_v = 1$, so the magnitude of the current fundamental harmonic is quite higher than the amplitudes of the higher harmonics; as a result, the measured current is sinusoidal. Concerning the $P1$ strategy, as predicted previously observing Fig. 3(b), the higher V_o/V_i gain values when k increases, (compared with the corresponding values using a nominal load resistance) are able to strongly limit the influence of the higher harmonics in the final waveform, making it to that one provides using the $P2$ strategy.

In Fig. 8, the Total Harmonic Distortion (THD) of the primary current at different coupling coefficients, referring to the results shown in Fig. 6 is shown. As expected, the THD is extremely low for the control strategy $P2$ independent of the coupling coefficients. On the other hand, using $P1$, the THD increases significantly for higher coupling coefficients, i.e. $k = 0.3$ and $k = 0.5$. Obviously, the THD for the $P1$ strategy significantly improves when the load resistance increases.

So, it can be concluded that, while the P2 strategy grants in resonant conditions, independently by the load, a sinusoidal current, which gives the possibility to use the FHA without approximation, the P1 strategy shows critical issues especially when a high load

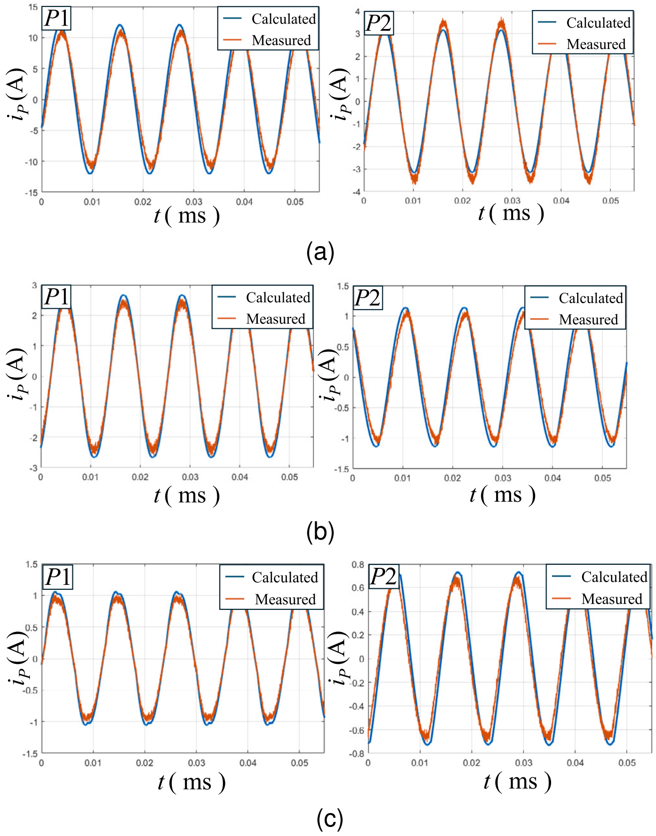

Fig. 7. Comparison between measured and predicted primary current using $P1$ and $P2$ design procedures. (a) k = 0.1; (b) k = 0.3; (c) k = 0.5.

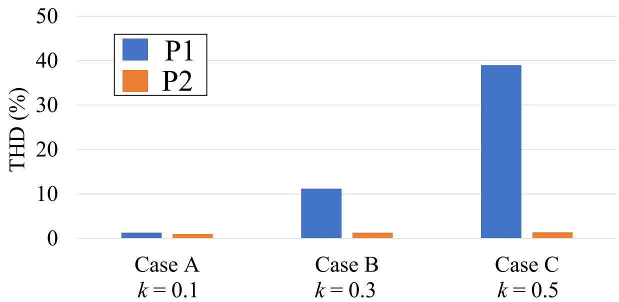

Fig. 8. Comparison of primary current THD at different coupling coefficients.

(low load resistance) is set. In this condition, using FHA to model the converter drives to approximations has a negative impact on the dynamic performances of the converter, as will shown in the next paragraph.

4.2. Transient validation

To evaluate the accuracy of the dynamic model a closed-loop control has been implemented, as shown in Fig. 9.

Firstly, the output voltage to frequency transfer function $T_p(s) = V_o(s)/\omega(s)$ has been obtained from the small-signal model, using (27). The Bode diagrams of T_p calculated for the three different coupling coefficients and using $P1$ and $P2$ are shown in Fig. 10(a) and (b) respectively.

Then, the controller $C(s)$ has been designed to achieve the desired response. Due to their good compromise between performance and simplicity, PI controllers have been chosen

$$C(s) = K_p + K_i \frac{1}{s} \tag{30}$$

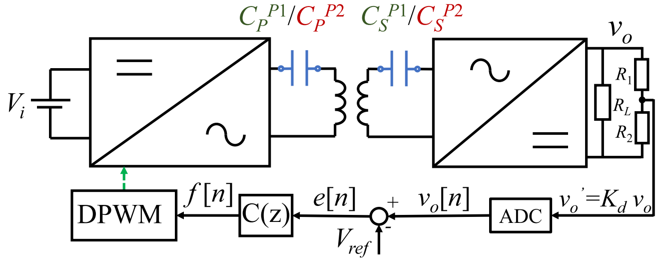

Fig. 9. Comparison of primary current THD at different coupling coefficients.

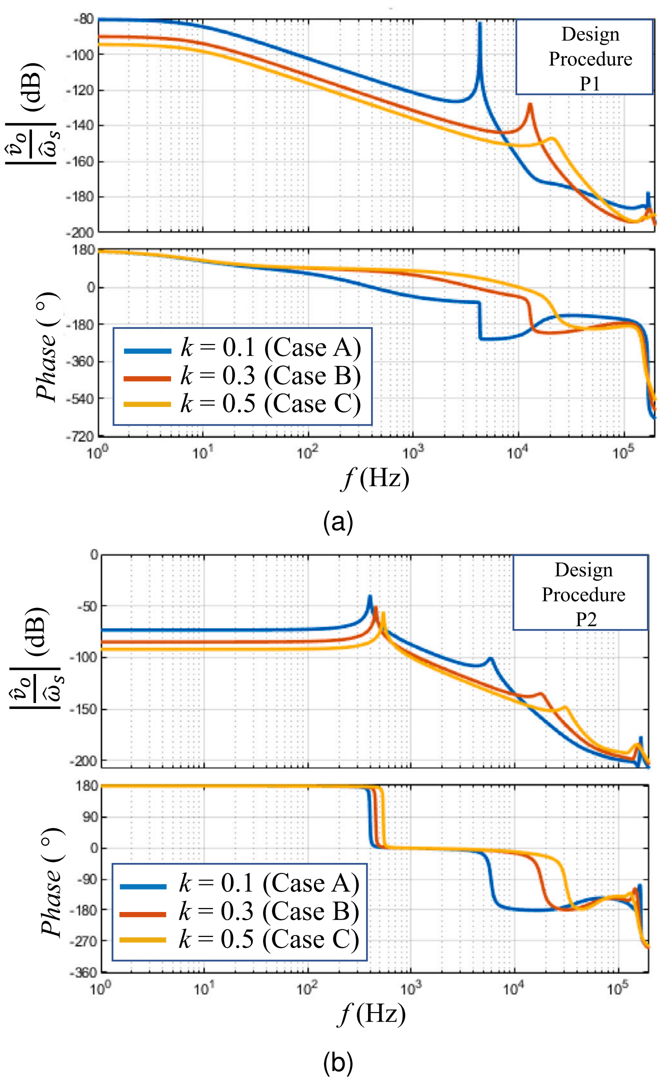

Fig. 10. Frequency to output voltage Bode diagrams for three different coupling coefficients. (a) Designing the system using $P1$. (b) Designing the system using $P2$.

The coefficients have been chosen using PID Tuner by MATLAB choosing a Bandwidth $BW = 175$ rad/s and Phase Margin PM=60°.

Once $C(s)$ has been designed, the controllers have been discretized using the Tustin transformation since this method preserves both the gain and phase properties of the controller below 1/10 of the sampling frequency. This task is obtained using the transformation:

$$s = \frac{2}{T_s}\frac{z-1}{z+1} \tag{31}$$

where T_s is the ADC sampling frequency and it has been set to $T_s = 11.7$ μs. Since the ADC has an input voltage range (0–3.3)V, a voltage divider has been used. Since the maximum output voltage is $V_o^{max} = 12$ V, the gain of the voltage divider has been set to $K_d = 0.275$. The PWM signal is then generated by a timer and, the operating frequency f_s at step n, is updated according to the control law:

$$f[n] = p[n] + i[n] \tag{32}$$

where

$$p[n] = K_p e[n] \tag{33}$$

$$i[n] = \frac{K_i T}{2}(e[n] + e[n-1]) + i[n-1] \tag{34}$$

with $e[n] = v_o[n]$-$v_o[n-1]$.

The procedure shown in the previous lines is well known; its potential is related to the fact that using a simple approach to model the converter, based on FHA approximation, it is possible to design a control strategy based on a PID controller, which is typically simple to be used, to realize powerful control strategies. Obviously, the accuracy of the control strategy is depending by the accuracy of the model; this is reason why the $P1$ strategy, working with a low load resistance, could give problems with high k values (where the FHA approximation is not so valid in practice). Two closed-loop tests have been performed on a converter working with a nominal load resistance. The first one consists on provide a step change of DC input voltage V_{DC} from 3 V to 6 V. The results are shown in Fig. 11, where the red line is the response of the controller designed with $P1$ while the blue line is when designed with $P2$. In particular, in Fig. 11(a), (b) and (c), the responses when the systems operate with $k = 0.1$, $k = 0.3$ and $k = 0.5$ are shown. The settling time that requires the system's output voltage to reach and stay within a certain 10% of tolerance range around its final value after the change of input voltage input is shown. As can be seen in Fig. 11(a), for low values of coupling coefficients, i.e. $k = 0.1$, the settling time of the controller's response is approximately $t_{s1} = t_{s2} = 525$ ms. Increasing the coupling coefficient, i.e. $k = 0.3$, the procedure $P2$ starts to perform better, producing a settling time $t_{s2} = 586$ ms respect to $t_{s2} = 586$ ms of the $P1$ procedure, as shown in Fig. 11(b). The $P2$ procedure performs much better for high coupling coefficients, i.e., for $k = 0.5$, as shown in Fig. 11(c). In this case, the settling time using the procedure $P2$ is $t_{s2} = 657$ ms against the longer settling time of procedure $P1$ $t_{s2} = 1213$ ms.

The dynamic performance degradation for high coupling coefficients of the system sized using $P1$ is also confirmed by measuring the output voltage transient when the reference voltage is changed from 3 V to 6 V at different coupling coefficients while maintaining the input voltage at $V_{DC} = 12$V, as shown in Fig. 12. The case with $k = 0.1$ is shown in Fig. 12(a), where the two procedures reach the new steady-state value approximately with the same time, respectively $t_{s1} = 261$ ms and $t_{s2} = 234$ ms. Increasing the coupling coefficient the performance of designing the system with P2 fastly decreases. For example, for $k = 0.5$, the settling time using $P2$ is approximately the six times longer than using $P1$, since $t_{s1} = 236$ ms while $t_{s2} = 1245$ ms.

For this reason, designing the system using $P2$ is possible to maintain excellent dynamic performance also when the system operates at a high coupling coefficient. On the other hand, using $P1$ and operating at a high coupling coefficient allow to maintain the stability of the system but the dynamic performance is significantly lower than $P2$.

5. Conclusions

The comparison between the two sizing techniques has led to interesting application implications. Although at first the difference between the two procedures may seem irrelevant, the consequences on the behavior of the system are significant.

The main conclusions emerging from this work can be summarized as follows:

- The procedure $P2$ allows for $M_v = 1$ at $f_s = f_n$, independently by the coupling coefficients. On the other hand, using $P1$ the voltage gain M_V is significantly reduced for high coupling coefficients. Thus, for those applications where unity gain is required at the nominal frequency, the use of $P2$ seems to be preferable.
- For applications where ensuring maximum efficiency at the nominal working frequency is necessary, procedure $P1$ seems to be preferable. In fact, the procedure $P1$ always allows to operate in resonance at the nominal frequency, achieving the maximum efficiency. On the other hand, using $P2$ this condition is not guaranteed.
- For applications where dynamic control must be particularly rapid, designing the system with procedure $P2$ seems to be preferable as it ensures a lower presence of harmonics, making small-signal models highly accurate. On the other hand, when designing the system with procedure $P1$ and operating with high coupling coefficients, we found that the presence of harmonics degrades the model's accuracy and consequently the controller performance.

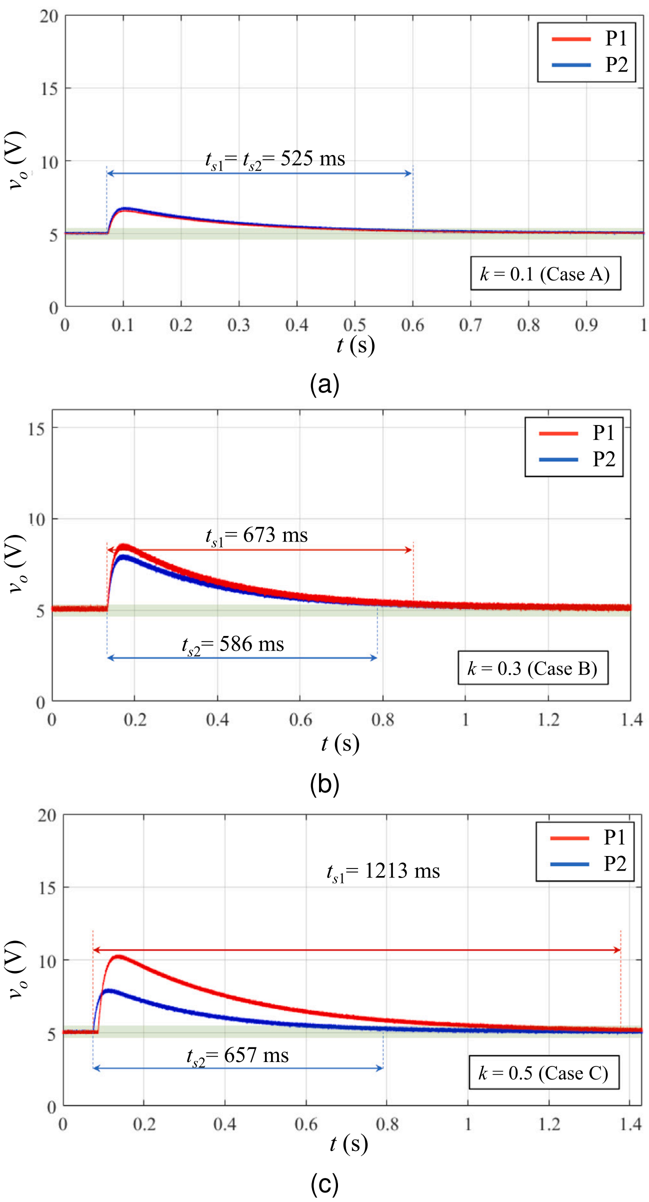

Fig. 11. Output voltage transients during input voltage step change from V_{DC} = 3V to V_{DC} = 6 V. The red trace is output voltage when the system is designed with $P1$ while the blue trace is the output voltage when the system is designed with $P2$. (a) Variation with k = 0.1. (b) Variation with k = 0.3. (c) Variation with k = 0.5.

Declaration of competing interest

The authors declare that they have no known competing financial interests or personal relationships that could have appeared to influence the work reported in this paper.

Data availability

No data was used for the research described in the article.

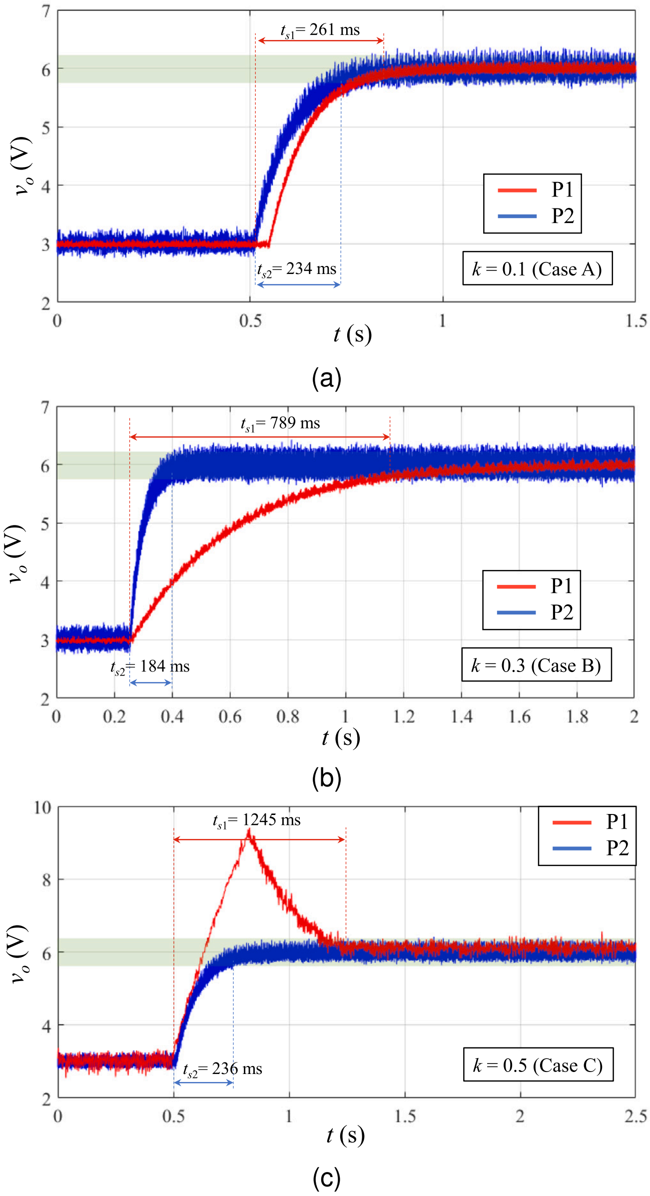

Fig. 12. Output voltage reference tracking transient using the two different design procedures. The red trace is the output voltage when the system is designed with $P1$ while the blue trace is the output voltage when the system is designed with $P2$. (a) Reference tracking with $k = 0.1$. (b) Reference tracking with $k = 0.3$. (c) Reference tracking with $k = 0.5$.

References

[1] Mude KN, Aditya K. Comprehensive review and analysis of two-element resonant compensation topologies for wireless inductive power transfer systems. Chin J Electr Eng 2019;5(2):14–31. http://dx.doi.org/10.23919/CJEE.2019.000008.

[2] Zhang W, Mi CC. Compensation topologies of high-power wireless power transfer systems. IEEE Trans Veh Technol 2016;65(6):4768–78. http://dx.doi.org/10.1109/TVT.2015.2454292.

[3] Xu Jin, Xu Yuhui, Zhang Qian. Calculation and analysis of optimal design for wireless power transfer. Comput Electr Eng 80. http://dx.doi.org/10.1016/j.compeleceng.2019.106470.

[4] Torchio R, Cirimele V, Alotto P, Freschi F. Modelling of road–embedded transmitting coils for wireless power transfer. Comput Electr Eng 2020;88. http://dx.doi.org/10.1016/j.compeleceng.2020.106850.

[5] Patil D, McDonough MK, Miller JM, Fahimi B, Balsara PT. Wireless power transfer for vehicular applications: Overview and challenges. IEEE Trans Transp Electr 2018;4(1):3–37. http://dx.doi.org/10.1109/TTE.2017.2780627.

[6] Zhang Z, Pang H, Georgiadis A, Cecati C. Wireless power transfer—An overview. IEEE Trans Ind Electron 2019;66(2):1044–58. http://dx.doi.org/10.1109/TIE.2018.2835378.

[7] Onai K, Ojo JO. Performance analysis and design of frequency controlled series-series compensated inductive power transfer system for electric vehicle battery charging. IEEE Trans Ind Appl 2022;58(1):962–73. http://dx.doi.org/10.1109/TIA.2021.3130845.
[8] Zhang J, Zhao J, Mao L, Zhao J, Jiang Z, Qu K. ZVS operation of class-E inverter based on secondary side zero compensation switching at variable coupling coefficient in WPT. IEEE Trans Ind Appl 2022;58(1):1022–31. http://dx.doi.org/10.1109/TIA.2021.3125916.
[9] Xu Jin, Tian Qiyu. Continuous power regulation in wireless power transfer system with a new magnetic field superposition transmitter. Comput Electr Eng 2021;90. http://dx.doi.org/10.1016/j.compeleceng.2021.106970.
[10] Zhang W, Wong S-C, Tse CK, Chen Q. Design for efficiency optimization and voltage controllability of series–series compensated inductive power transfer systems. IEEE Trans Power Electron 2014;29(1):191–200. http://dx.doi.org/10.1109/TPEL.2013.2249112.
[11] Frechter Y, Kuperman A. Output voltage range of a power-loaded series–series compensated inductive wireless power transfer link operating in load-independent regime. IEEE Trans Power Electron 2020;35(6):6586–93. http://dx.doi.org/10.1109/TPEL.2019.2953200.
[12] Vulfovich A, Kuperman A. Design space of sub-resonant frequency- controlled series–series-compensated inductive wireless power transfer links operating with constant output current under frequency constraints. IEEE J Emerg Sel Top Power Electron 2022;10(5):5414–22. http://dx.doi.org/10.1109/JESTPE.2022.3179724.
[13] Chen Y, et al. A unipolar-duty-cycle hybrid control strategy of series–series compensated IPT system for constant-current output and efficiency optimization. IEEE Trans Power Electron 2022;37(11):13884–901. http://dx.doi.org/10.1109/TPEL.2022.3173041.
[14] Kuperman A. Compensation capacitors sizing for achieving arbitrary load-independent voltage gain in series-series inductive WPT link operating at fixed frequency. IEEE Trans Power Deliv 2020;35(6):2737–9. http://dx.doi.org/10.1109/TPWRD.2020.2995117.
[15] Kuperman A. Simple enhancement of series–series-compensated inductive wireless power transfer links operating with load-independent voltage output at fixed frequency to attain zero inverter phase angle. IEEE Trans Power Electron 2023;38(5):5670–4. http://dx.doi.org/10.1109/TPEL.2023.3241107.
[16] Corti F, et al. A secondary-side controlled electric vehicle wireless charger. Energies 2020. http://dx.doi.org/10.3390/en13246527.
[17] Moosavi SA, Mortazavi SS, Namadmalan A, Iqbal A, Al-Hitmi M. Design and sensitivity analysis of dynamic wireless chargers for efficient energy transfer. IEEE Access 2021;9:16286–95. http://dx.doi.org/10.1109/ACCESS.2020.3048029.
[18] Zhang Y, Chen S, Li X, Tang Y. Design methodology of free-positioning nonoverlapping wireless charging for consumer electronics based on antiparallel windings. IEEE Trans Ind Electron 2022;69(1):825–34. http://dx.doi.org/10.1109/TIE.2020.3048322.
[19] Huang M, Lu Y, Martins RP. A reconfigurable bidirectional wireless power transceiver for battery-to-battery wireless charging. IEEE Trans Power Electron 2019;34(8):7745–53. http://dx.doi.org/10.1109/TPEL.2018.2881285.
[20] Zahid ZU, et al. Modeling and control of series–series compensated inductive power transfer system. IEEE J Emerg Sel Top Power Electron 2015;3(1):111–23. http://dx.doi.org/10.1109/JESTPE.2014.2327959.
[21] Bertolini V, Corti F, Cardelli E, Reatti A. Control strategies for output voltage regulation in a SS compensated wireless charging system. In: 2022 IEEE 21st mediterranean electrotechnical conference. MELECON, Palermo, Italy; 2022, p. 896–901. http://dx.doi.org/10.1109/MELECON53508.2022.9842927.

Fabio Corti received the M.S. degree in electrical and automation engineering and the Ph.D. in industrial engineering from the University of Florence, Italy, in 2016 and 2019 respectively. He was postdoc research fellow at Consiglio Nazionale delle Ricerche (CNR) in 2019 and at the University of Perugia from 2020 to 2022. He is actually researcher at the University of Florence and his research interest includes modeling and control of DC–DC PWM and resonant converters, wireless power transfer and electric vehicle powertrain.

Vittorio Bertolini received the M.S. degree in mechanical engineering from the University of Perugia, Perugia, in 2021. He is currently a Ph.D. student in industrial engineering in the University of Perugia. His research interest includes modeling and control of DC–DC resonant converters and wireless power transfer.

Antonio Faba received the Electrical Engineering degree from the University of L'Aquila, L'Aquila, Italy, in 1998, and the Ph.D. degree in industrial engineering from the University of Perugia, Perugia, Italy, in 2006. He was a Full Professor with National Habilitation in 2018. He is currently an Associate Professor with the Department of Engineering, University of Perugia, Italy, where he is the Head of the Laboratory of Electromagnetic Characterization. Dr. Faba is a Member of the IEEE Magnetic Society.

Ermanno Cardelli received the M.Sc. degree in electrical engineering in 1981 and the Ph.D. degree in electrical engineering from the University of Pisa, Pisa, Italy in 1987. He is currently a Full Professor of Electric Engineering with the University of Perugia, and the Head of Department of Engineering. He is an author of more than 200 refereed technical papers, mainly on numerical techniques and modeling for the electromagnetic field analysis. He is an author of two Italian edited books and an international book chapter. Dr. Cardelli is the Past Chair of the IEEE Italy Section, the Chair of the Electrical Engineering Group. He is a General Chair in several international conferences and a Coordinator of many Italian and European Scientific Programs.

Alberto Reatti received the M.Sc. degree in electronics engineering from the University of Florence, Italy, in 1988, and the Ph.D. degree in electrical engineering from the University of Bologna, Italy, in 1993. In 1992, he was an Associate Researcher with the Department of Electrical Engineering, Wright State University, Dayton, OH, USA. He is currently Associate Professor and the President of Patent and Technology Transfer Board of University of Florence. His current research interests include high-frequency resonant and PWM dc–dc power converters, modeling and control of converters and renewable power sources.